Electronic Supplementary Material (ESI) for Journal of Materials Chemistry A.

Supporting Information

A nitrogen fixation strategy to synthesize NO via the thermally-assisted photocatalytic conversion of air

Yu Yu[a,†], Changhong Wang[a,†], Yifu Yu[a,*], Yanmei Huang[a], Cuibo Liu[a], Siyu Lu[c], Bin Zhang[a,b,*]

[a]Department of Chemistry, School of Science, Institute of Molecular Plus, Tianjin University, Tianjin 300072, China

[b]Tianjin Key Laboratory of Molecular Optoelectronic Sciences, Frontiers Science Center for Synthetic Biology (Ministry of Education), Tianjin University, Tianjin 300072, China

[c]Green Catalysis Center, College of Chemistry, Zhengzhou University, Zhengzhou 450000, China

[†]These authors contributed equally to this work.

***Corresponding authors**

E-mail: yyu@tju.edu.cn; bzhang@tju.edu.cn

Additional Results and Discussion

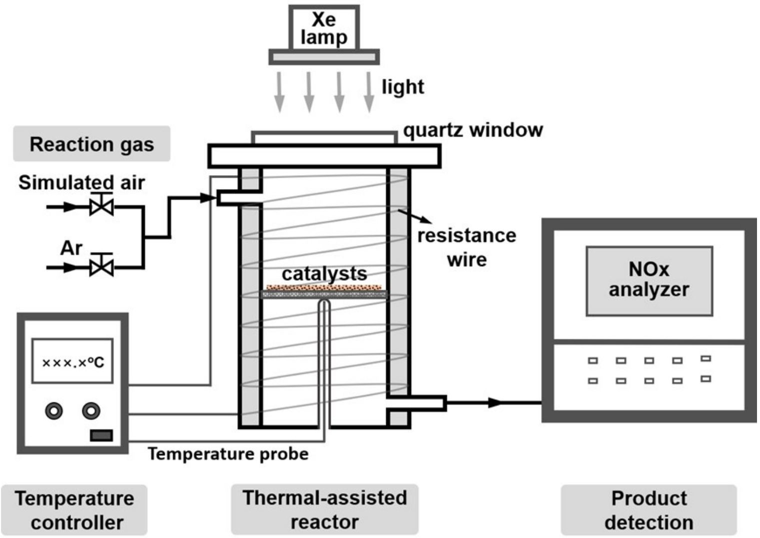

Scheme S1. Schematic illustration for the thermal-assisted photocatalytic N_2 oxidation reactor.

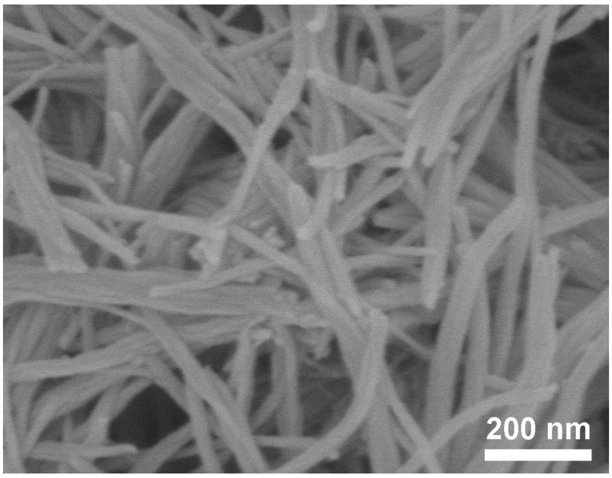

Fig. S1 SEM image of WO_3 nanorods

SEM image showed that WO_3 nanorods were produced on a large scale.

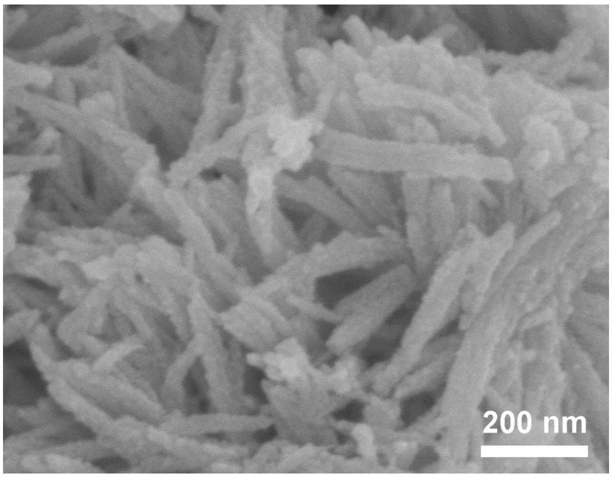

Fig. S2 SEM image of the TiO_2/WO_3 heterostructured nanorods. The surface of WO_3 nanorods becomes rough after growing TiO_2.

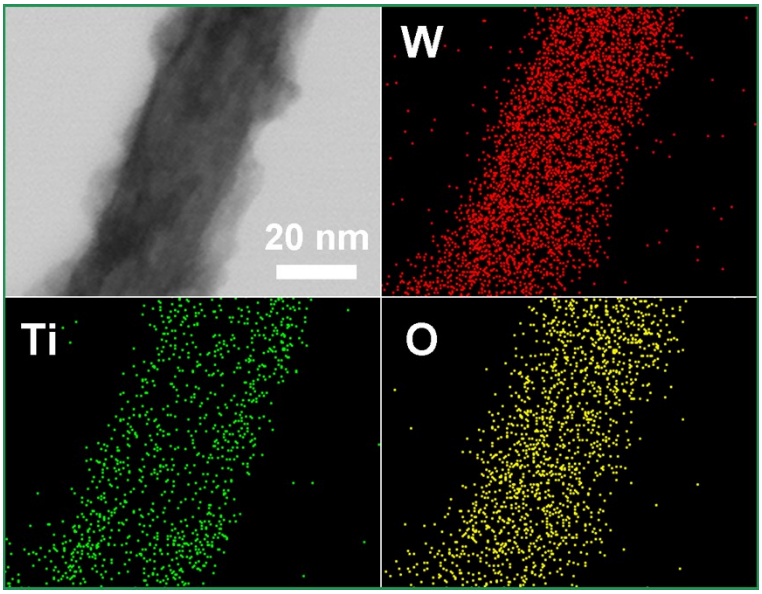

Fig. S3 Element mapping images of the TiO_2/WO_3 heterostructured nanorods.

STEM-EDS elemental mapping images revealed the elemental distribution. W and Ti elements distributed in core and shell, respectively, while oxygen existed in both core and shell. A thin layer of nanosheets coated on the WO_3 to produce the TiO_2/WO_3 heterostructured nanorods.

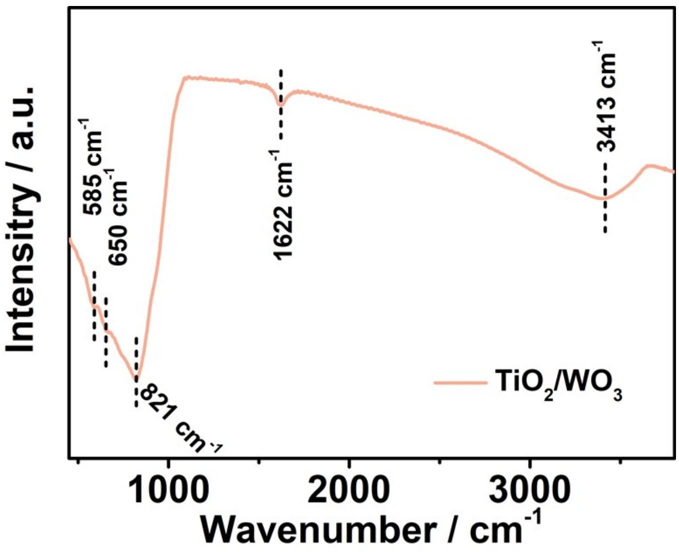

Fig. S4 FTIR spectrum of the TiO_2/WO_3 heterostructured nanorods.

The peaks located at 3413 and 1622 cm^{-1} were due to the stretching and bending vibrations of the surface adsorbed water molecules. And the peaks located at 585 and 650 cm^{-1} were attributed to the stretching vibrations of Ti-O bond in TiO_2. Moreover, the W-O stretching and vibration bands in the region 960 cm^{-1} to 800 cm^{-1} were also detected.

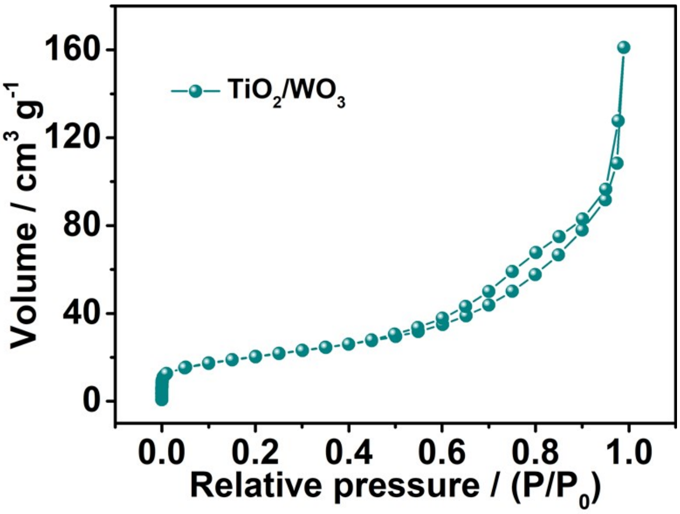

Fig. S5 N_2 adsorption-desorption isotherm for TiO_2/WO_3 heterostructured nanorods.

The BET surface area of TiO_2/WO_3 heterostructured nanorods was calculated to be 72.0 m^2 g^{-1} .

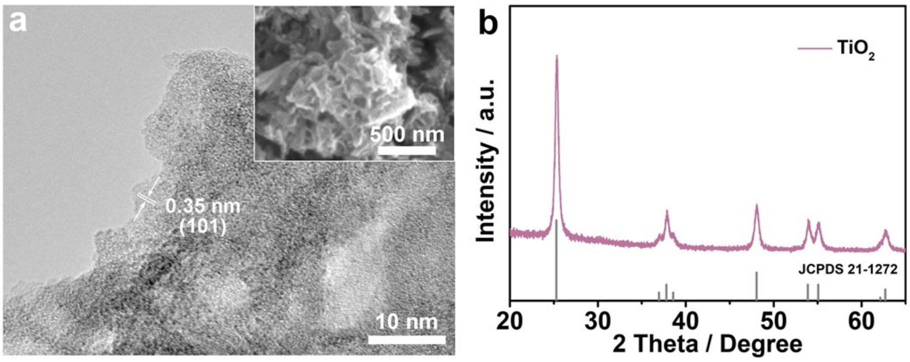

Fig. S6 (a) HRTEM image (inset is the SEM image) and (b) XRD pattern of TiO_2 nanosheets.

SEM image (inset in Fig. S6a) showed the assembled nanosheet structure of TiO_2 nanosheets. HRTEM image (Fig. S6a) displayed the crystal structure of nanosheets with TiO_2 (101) plane. X-ray diffraction (XRD) pattern (Fig. S6b) further proved the nanosheets as pure TiO_2 (JCPDS No. 21-1272).

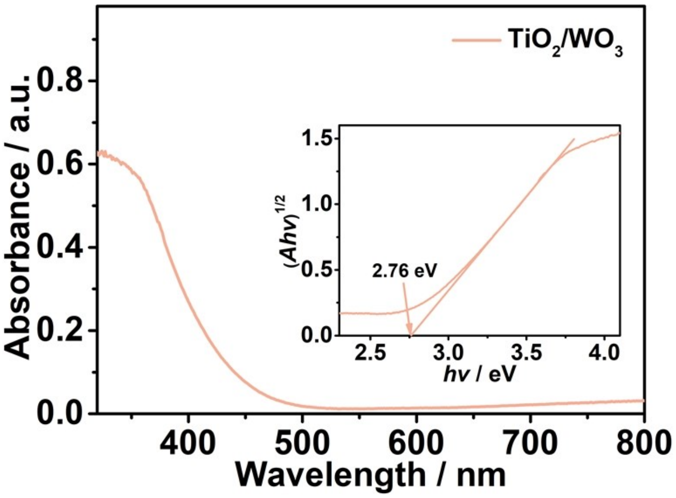

Fig. S7 UV-Vis absorbance spectra and the Tauc plots (inset) of the TiO_2/WO_3 heterostructured nanorods.

The intercepts of extrapolated straight lines of Tauc plots showed the corresponding bandgaps (2.76 eV) of the TiO_2/WO_3 heterostructured nanorods.

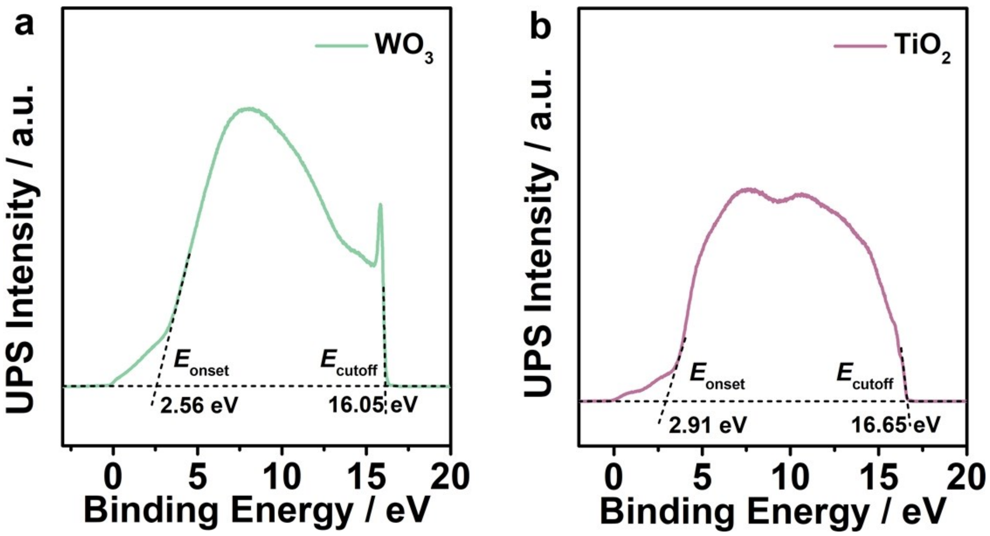

Fig. S8 UPS spectra of (a) WO_3 nanorods and (b) TiO_2 nanosheets.

Ultraviolet photoelectron spectroscopy (UPS) was used to determine the ionization potential [equivalent to the valence band energy (E_v)] of WO_3 nanorods and TiO_2 nanosheets, which was calculated to be 7.48 eV and 7.73 eV by subtracting the width of the He I UPS spectra from the excitation energy (21.22 eV). The detailed calculations were shown as follows:

The E_v versus vacuum level (eV) = 21.22 eV – (E_{cutoff} - E_{onset})

The E_v versus NHE (V) = (The E_v versus vacuum level -4.85) (V) (pH = 7)

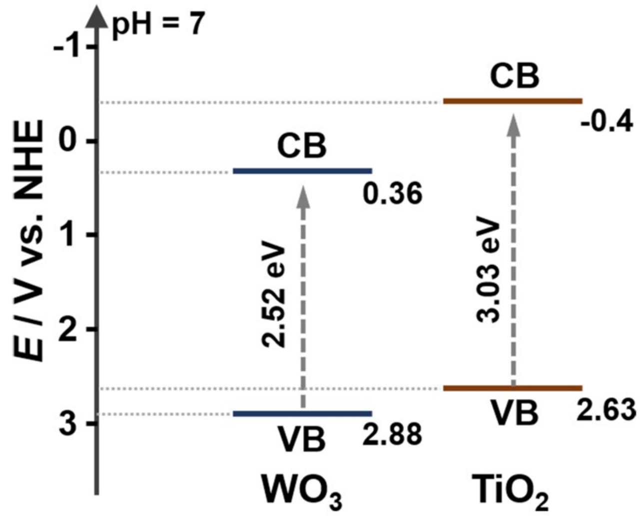

Fig. S9 The schematic diagram for the band structures of WO_3 nanorods and TiO_2 nanosheets.

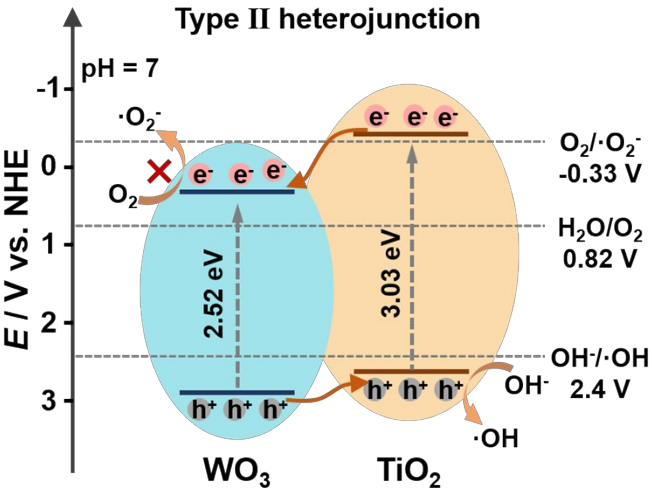

Fig. S10 Schematic illustration for the charge-carriers migration according to the type-II heterojunction mechanism in the TiO_2/WO_3 heterostructured nanorods.

Considering that the CB potential of WO_3 was more positive than the standard potential of $O_2/\cdot O_2^-$ (-0.33 V vs NHE), no obvious $\cdot O_2^-$ signal should be observed if the photogenerated charge-carriers migration followed the type-II heterojunction mechanism.

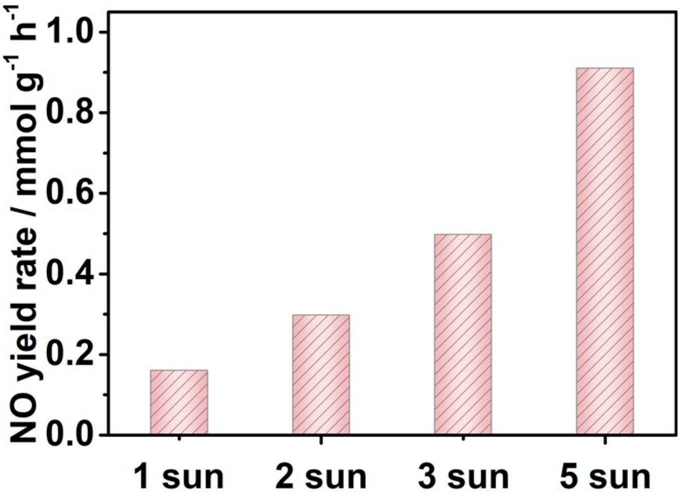

Fig. S11 NO yield rate under different illumination intensity at 300 °C.

The yield rate of NO increased obviously with the increase of the illumination intensity from 1 sun to 5 sun.

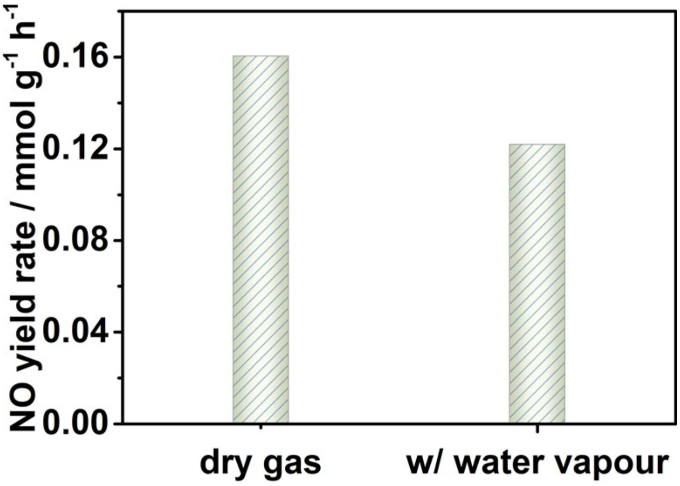

Fig. S12 Effect of water vapour on the yield rate of NO.

The yield rate of NO using the wet simulated air as the feed gas under 1 sun illumination at 300 ^{o}C was 0.12 mmol g^{-1} h^{-1}, which was slight lower than that using the dry simulated air as the feed gas (0.16 mmol g^{-1} h^{-1}).

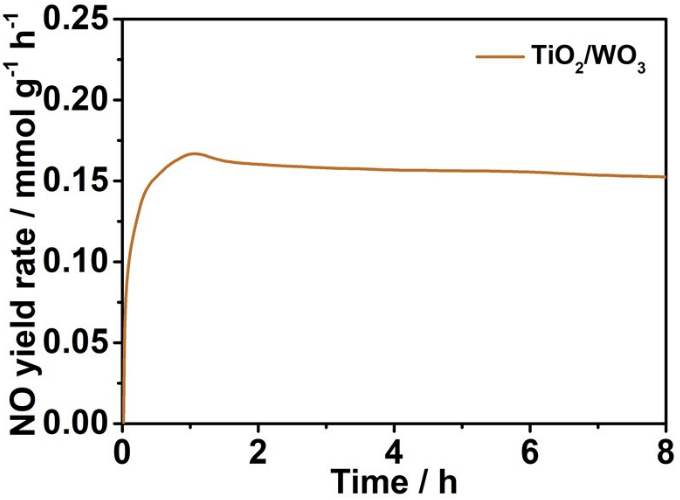

Fig S13. The time-dependent yield rate of NO over TiO_2/WO_3 heterostructures for continuous 8 hours test.

No obvious decline can be seen for the yield rate of NO, suggesting the well stability of the TiO_2/WO_3 heterostructures for photocatalytic oxidation of nitrogen.

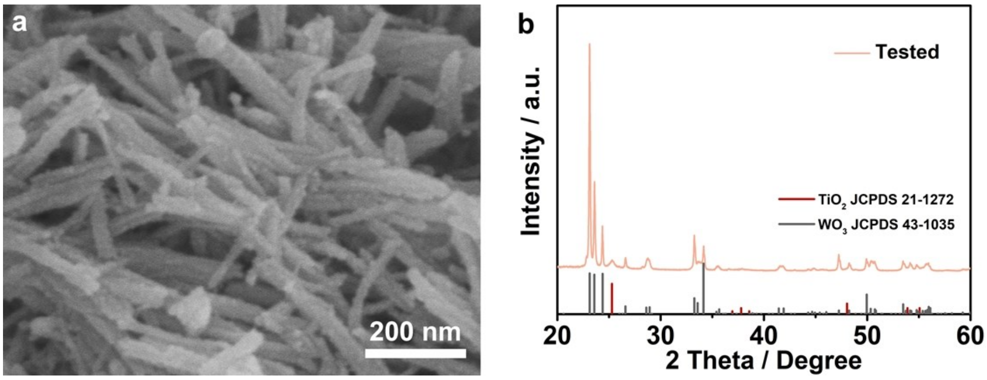

Fig. S14 (a) SEM image and (b) XRD pattern of the TiO_2/WO_3 heterostructured nanorods after 8 hours test.

The morphology and crystalline structure of the TiO_2/WO_3 heterostructured nanorods maintained well after long-term test.

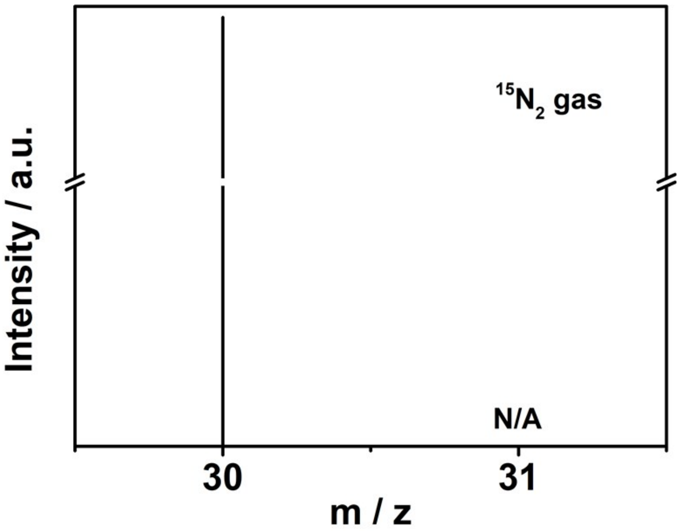

Fig. S15 Mass spectra of GC-MS analysis of the in the $^{15}N_2$ gas for the isotope experiment.

No ^{15}NO (m/z = 31) was detected in the $^{15}N_2$ gas.

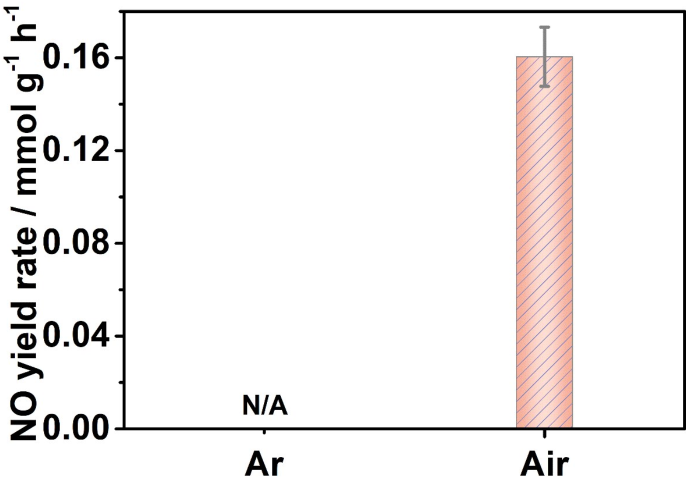

Fig. S16 Blank experiment: yield rate of NO production using different gas as the reactant.

No NO was detected in the argon atmosphere.

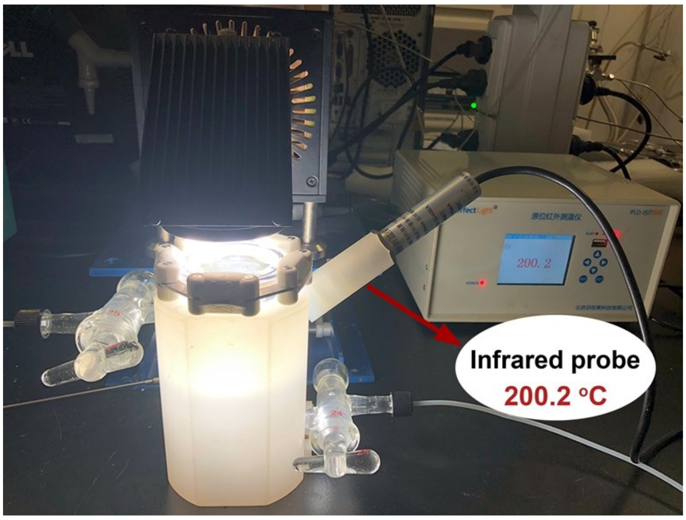

Fig. S17 Photograph of the device for photocatalytic N_2 oxidation under 10 sunlight illumination equipped with infrared thermometer for the detection of temperature on the surface of catalysts.

The temperature at the photocatalyst surface could achieve 200 °C as the incident light intensity was 10 sun.

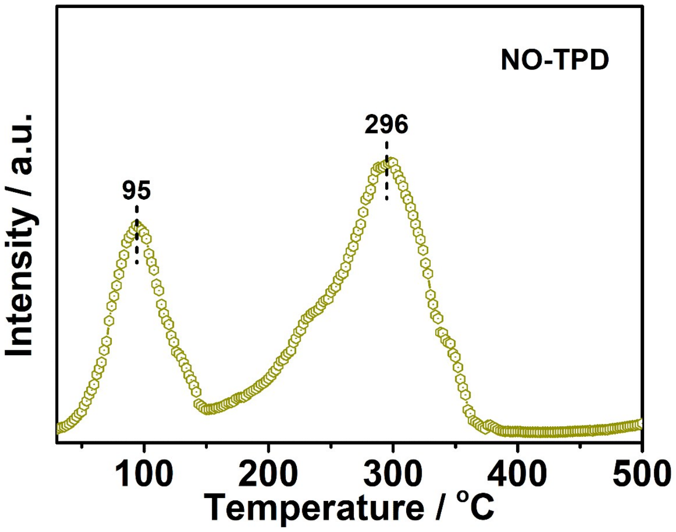

Fig. S18 Temperature programmed desorption (TPD) profile of NO over TiO_2/WO_3 heterostructures.

In the NO TPD profile, there were two peaks at about 95 °C and 296 °C, which were attributed to the physical adsorption and chemical adsorption of NO on the TiO_2/WO_3 heterostructures, respectively.

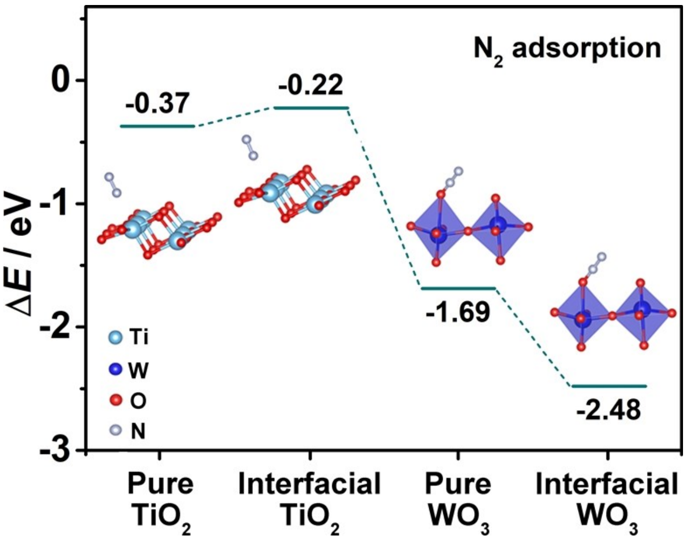

Fig. S19 N_2 adsorption energies on different samples.

Pure WO_3 (-1.69 eV) and interfacial WO_3 in TiO_2/WO_3 heterostructures (-2.48 eV) showed more negative adsorption energies than those of pure TiO_2 (-0.37 eV) and interfacial TiO_2 in TiO_2/WO_3 heterostructure (-0.22 eV). This result revealed that N_2 photooxidation proceeded on the surface of WO_3 in the TiO_2/WO_3 heterostructures and interfacial charge transfer facilitated N_2 adsorption.

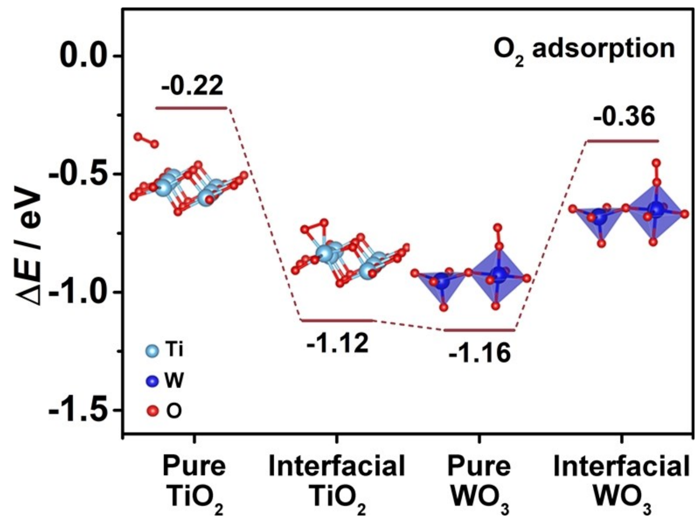

Fig. S20 O_2 adsorption energies on different sample surfaces.

In the TiO_2/WO_3 heterostructure, the interfacial TiO_2 showed more negative adsorption energy of O_2 (-1.12 eV) than that of interfacial WO_3 (-0.36 eV), indicating that O_2 showed preferential adsorption on the interfacial TiO_2 and further reduced by the photoelectrons under irradiation.

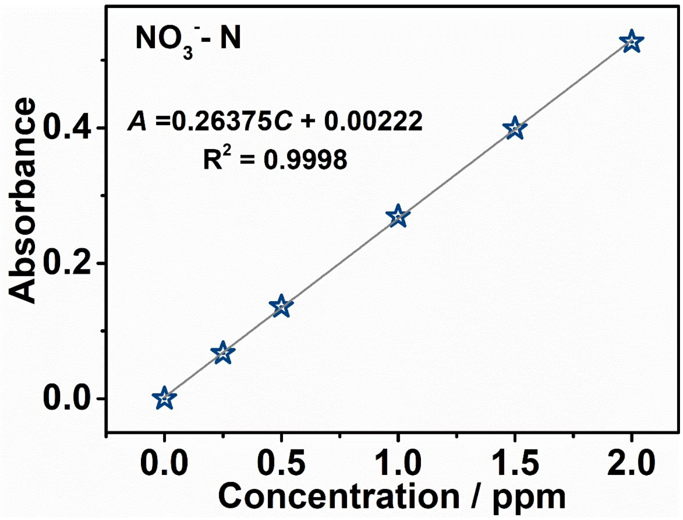

Fig. S21 The UV-Vis absorption spectra and the corresponding calibration curves of NO_3^--N.

The calibration curves showed good linearity.

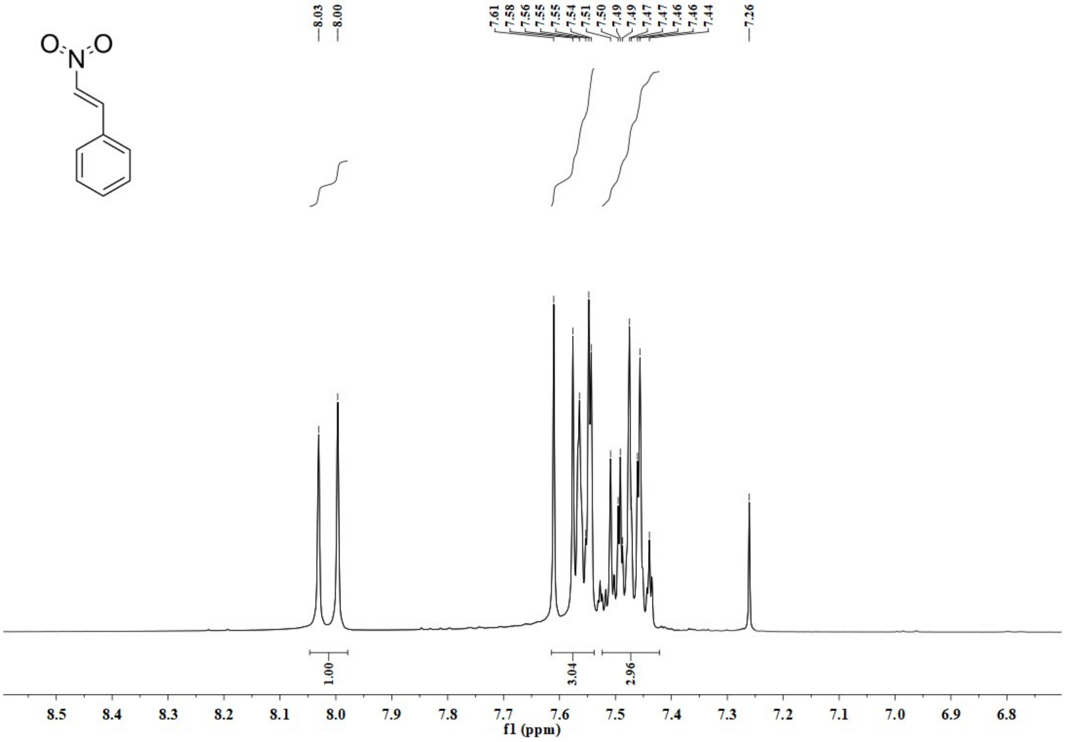

Fig. S22 NMR spectrum of the β-Nitrostyrolene product.

^{1}H NMR (400 MHz, $CDCl_3$) δ [ppm] 8.01 (d, J= 13.6, 1H),7.56 (m, 3H), 7.48 (m, 3H);

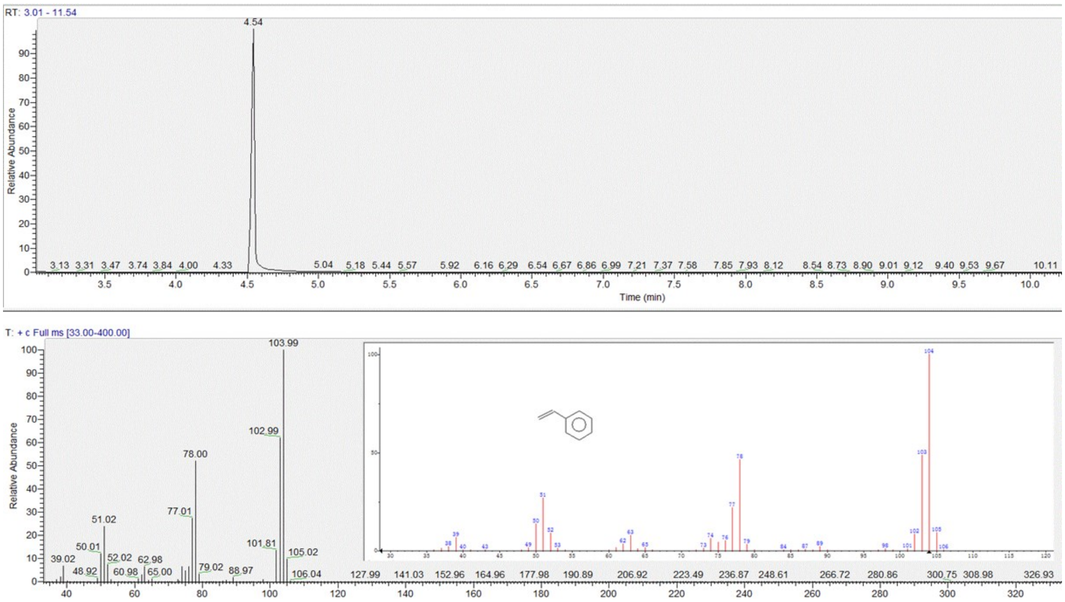

Fig. S23 GC spectrum of the product after the test with the Ar gas as the raw material.

No *β*-Nitrostyrolene product generated in the organic solvent system when Ar gas was used as the raw material for photocatalysis.